Advances in Monte Carlo Simulation for Light Propagation in Tissue

Vijitha Periyasamy and Manojit Pramanik

Abstract—**Monte Carlo (MC) simulation for light propagation in tissue is the gold standard for studying the light propagation in biological tissue and has been used for years. Interaction of photons with a medium is simulated based on its optical properties. New simulation geometries, tissue-light interaction methods, and recording techniques recently have been designed. Applications, such as whole mouse body simulations for fluorescence imaging, eye modeling for blood vessel imaging, skin modeling for terahertz imaging, and human head modeling for sinus imaging, have emerged. Here, we review the technical advances and recent applications of MC simulation.**

Index Terms—**Biomedical optical imaging, computational modeling, light tissue interaction, Monte Carlo (MC) simulation, photon propagation, tissue optics.**

I. INTRODUCTION

SCIENTISTS are always looking for new bioimaging modalities. Optical imaging is a strong contender owing to its use of nonionizing radiation and noninvasive use [1]. Diffuse reflectance spectroscopy (DRS), near-infrared spectroscopy (NIRS), diffuse optical tomography (DOT), Raman imaging, fluorescence imaging, optical microscopy, optical coherence tomography (OCT), and photoacoustic (PA) imaging are some of the widely used biomedical optical imaging techniques for noninvasive imaging [2]. Optical window from 400 to 1400 nm is widely used, especially for deep tissue imaging [3], [4]. In each of these optical imaging modalities, the interaction between light and the biological medium (tissue) can be different. The light propagation inside the biological medium is characterized by strong scattering and absorption. The light that propagates back to the illuminating surface is studied in many optical imaging modalities, for example, in DRS, NIRS, OCT, etc. Photons can undergo either elastic or inelastic scattering in the tissue. The inelastic scattering carries the molecular signature of the medium and is used in Raman imaging. Emission of red-shifted (or Stokes shifted) light by the medium, is used to form fluorescent image. In OCT, the reflected light, which is coherent

with the illuminated source, interferes constructively and gives information about the depth as well as the reflectivity of the tissue. In PA imaging (PAI), the tissue undergoes thermoelastic expansion when the illuminated pulsed light is absorbed by the chromophores to produce pressure waves (in the form of ultrasound) [5]. All these different types of interactions between light and tissue need to be well understood to optimize and develop the various optical imaging techniques.
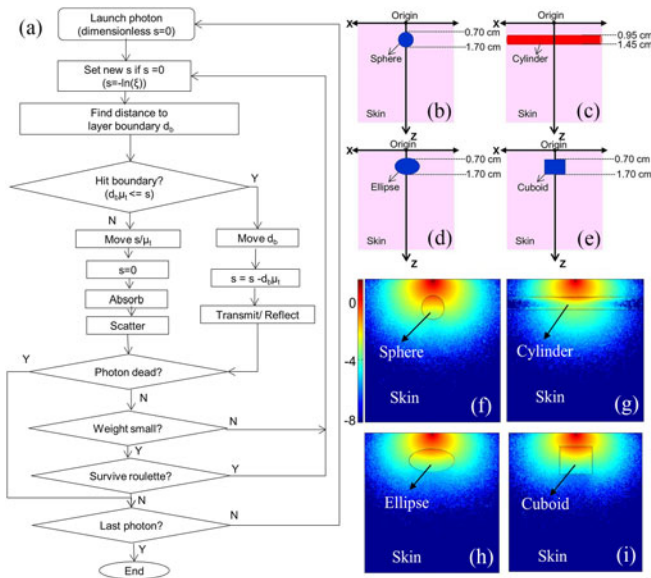
The radiative transfer equation (RTE) can be used to model the light propagation in a medium. Analytical solution for solving the RTE exists for simple cases. However, for more realistic media, with complex multiple scattering effects, numerical methods are required. Several numerical solutions for RTE with approximation have been proposed, but effective solutions for heterogeneous medium (tissue) still remain a challenge [6]. Hence, numerical simulation techniques have been designed for light propagation in tissue. Photon propagation in tissue is numerically simulated using Monte Carlo (MC) technique. MC is a stochastic modeling technique earlier used for radiation transport, which was introduced for light propagation [1], [7]. Here, the photon trajectory is predicted by persistent random walk. The method estimates ensemble-averaged quantities. MC was combined with diffusion theory (hybrid MC) for better accuracy near the light sources, where the diffusion theory fails [8]. The use of MC for light propagation in tissue was proposed by Wilson, but the implementation details of MC for light propagation in tissue were discussed a decade later [7].

Wang *et al.* were the first to discuss the programming steps of MC simulation for light propagation in multilayered tissue (MCML) coded in standard C, which is used widely even today due to its user-friendliness [9]. Tetrahedron-based inhomogeneous Monte Carlo optical simulator (TIM-OS) developed in C++, voxel-based MC (vMC) written in MATLAB, MC eXtreme written in compute unified device architecture (CUDA), and mesh-based MC (MMC) coded in MATLAB were developed for inhomogeneous simulation geometries [10]–[14]. In these numerical simulations, the photon travels through the defined medium in random steps. Physical quantities such as diffused reflectance, transmittance, and absorbance are estimated by tracking large number of photons through the medium [1]. There has been a review article covering the topic of MC over the years published several years ago [15]. Here, in this review, we revisit the concept of MC simulations, along with the discussions on the advancements in the simulation techniques and their new applications in biomedical imaging. Steps involved in tracking of photons in tissue using MC are discussed in

Fig. 1. (a) Block diagram of MCML as proposed by Wang *et al.* Reproduced with permission from [9]. (b)–(e) Sphere, cylinder, ellipsoid, and cuboid embedded in MCML with mismatched refractive index. (f)–(i) Absorbance maps of sphere, cylinder, ellipsoid, and cuboid embedded in MCML with mismatched refractive index. Reproduced with permission from [17].

Section II. Section III discusses various methods of describing the regular and irregular mediums for simulation. Light illumination patterns are discussed in Section IV. In Section V, MC for various optical imaging techniques are reviewed. Sections VI and VII are regarding the photon handling at the refractive surface and advances in recording of the photon. Optimization of MC and its applications are discussed in Sections VIII and IX, respectively. Finally, discussions are given in Section X.

II. BACKGROUND OF MC SIMULATION ALGORITHM

In MC simulation, a large number of photons are propagated through the simulation medium (tissue). Photons undergo reflection, refraction, absorption, and scattering [16]. Optical properties of the medium such as refractive index (n), absorption coefficient (μ_a), scattering coefficient (μ_s), and scattering anisotropy (g) determine the path traced by the photons. Absorption coefficient (μ_a) is defined as the probability of photon absorption in a medium per unit (infinitesimal) path length [1]. This physical quantity is measured by Beer's law, which is given as $I(x) = I_0 e^{-\mu_a x}$, where x is the distance along the light propagation direction and I_0 is the light intensity at $x = 0$. Scattering coefficient (μ_s) is defined as the probability of light scattering in a medium per unit (infinitesimal) path length. Scattering anisotropy (g) is defined as the mean of the cosine of the scattering angle. Typical values for biological tissues are $\mu_a = \sim 0.1\,\text{cm}^{-1}$, $\mu_s = \sim 100\,\text{cm}^{-1}$, $g = 0.9$, and $n = 1.4$ [4].

The tracking of the photon in the medium is shown in Fig. 1(a) as a flow chart. The medium in which the light propagation is simulated can be defined as an infinite or semi-infinite geometry depending on the simulation need. Photons are launched

with unit weight (w) with the direction cosines along the z-axis. In case of refractive index mismatch between the launch medium and the propagation medium, the amount of specular reflectance $[R_{sp} = (\frac{n_0 - n_1}{n_0 + n_1})^2]$ is deducted from the weight of the photon $(w = 1 - R_{sp})$, and then it is refracted. In case of matched boundary conditions, the weight of the photon entering the medium is 1. Then, the photon takes a random step-size $(s = -\frac{\ln \xi}{\mu_a + \mu_s}$, where ξ is the random number), and checks if the step-size is greater than the distance to the nearest boundary. If the photon does not hit the boundary, then it moves by the step-size to the new location and drops weight $(\Delta W = \frac{\mu_a}{(\mu_a + \mu_s)} W)$. For scattering, polar angle θ and azimuthal angle $\emptyset$ are randomly sampled based on which direction the cosines of the photon are recomputed. θ is computed using Henyey–Greenstein (HG) function, which is $p(\cos \theta) = \frac{1 - g^2}{2 \times (1 + g^2 - 2 \times g \times \cos \theta)^{3/2}}$ and $\emptyset = 2\pi \xi$. Absorption and scattering steps are repeated until the photon dies. Russian roulette is used to compensate for killing photons which are below a certain threshold weight. When the step-size is greater than the distance to the nearest boundary, the photon moves to the boundary, and then checks for transmission or reflection.

III. DEFINING THE MEDIUM

Representing the simulation geometry as a layered structure was most common and simple approach. Each layer represented one homogeneous part of the simulation medium. Regular-shaped objects such as sphere and cylinder that could be expressed as geometric/parametric equations were embedded in the planar model to mimic tumor, blood vessel, and so on. For applications which demanded higher accuracy, three-dimensional (3-D) magnetic resonance imaging (MRI) or computed tomography (CT) scans were required to obtain an accurate shape of the simulation geometry. These 3-D volumes were segmented and voxelated to obtain the simulation geometry to be used in MC [10]. In vMC, the photons were tracked through these voxels. To overcome the discrepancy at the curved boundaries, the simulation medium was segmented into nonuniform meshes. The density of these meshes could be controlled at the boundary; hence, it was feasible to do simulation in irregular shapes medium or inclusions.

A. Medium With Regular Shape

MCML written in standard ANSI C, propagated photons through a multilayered medium [9]. The simulation geometry was cylindrically symmetric about the z-axis. In conventional MCML, the simulation geometry was defined by the number of layers and the thickness of each layer [18]. In this model, the boundaries that the photon encounters were planes which were given by the plane equations. At each scattering site, the distance between the photon's current location (vector) and the plane (layer) in the direction of photon propagation was computed [7]. This kind of layer-based models have been used extensively due to their simplicity. For example, brain was approximated to five parallel layers and this approximation was used here to simulate the effect of increase in CSF on diffuse

reflected photons [19]. Monitoring of CSF volume was essential to monitor brain edema. Since the optical properties of brain vary during edema, applicability of NIRS for monitoring the same was proposed through MCML simulations. Skin is another organ which is widely approximated as layer structures. Skin was modeled as seven layers to study the effectiveness of optical clearing agents (OCA), such as glucose, propylene glycol, and glycerol, to increase the penetration depth of light for monitoring obesity and for photodynamic therapy of acne vulgaris [20], [21]. The study concluded that the layer of application of OCA changed the light absorption significantly only in the blue spectral range. In another study, skin was further approximated to a four-layer model to optimize the distance between the source and the detector in reflective pulse oximeter [22]. Optimal distance between the source and the detector was found to be 4 mm. This simulation also proved that introducing a Fresnel lens in the path of source–detector and skin enhanced the photopleythsmography signal by 140%.

1) Introduction of Embedded Objects: Multilayer model was a highly simplified model for many applications. Hence, MCML was further modified to incorporate objects of regular shapes, such as sphere and cylinder of matched refractive index to mimic tumor and blood vessels. The embedded object was defined by parametric equation. MCML was first modified to handle embedded objects of matched refractive index. Since there were errors in the observed output parameters, MCML was further modified to handle the refractive index mismatch for embedded objects of defined geometry, such as sphere, cylinder, ellipsoid, and cuboid (MCEO). The steps involved when photons hit the tissue-object boundary where they were either transmitted or reflected based on its refractive indices have been discussed by Periyasamy and Pramanik [17]. There was loss of accuracy in the results due to matched refractive index between the object (sphere or cylinder) and the surrounding layer. It was observed that there was an error of 5.76% when the refractive index mismatch was ignored (in case of lymph node modeled as sphere) [17], [27]. Similarly, error of 4.10% was observed on ignoring the refractive index between blood vessel (modeled as cylinder) and tissue. This error was 5.68% and 5.23% for ellipse and cuboid, respectively. Simulation geometry of embedded objects is shown in Fig. 1(b)–(e). The absorbance maps of the objects by MCEO are shown in Fig. 1(f)–(i).

Similarly, skin was modeled with blood vessels for imaging of port-wine stain [28]. Multiple cylinders with refractive index 1.33 were embedded within epidermis whose refractive index was 1.37 [28]. Photons were either refracted or transmitted when they encountered the blood vessels due to mismatched refractive indices. The angle of refraction was computed based on the angle of incidence which is detailed by Periyasamy and Pramanik [17]. Angle between the blood vessels was varied from 0°, 30°, 60°, and 90°. This angular orientation of the blood vessels was used to mimic cross-bridge blood vessels. Absorption map of cross-bridge blood vessels were projected on the plane $z = 0.25$ mm (which is the along the center of the 0° vessel). It was concluded that the location and angular orientation of the blood vessels influenced the energy distribution.
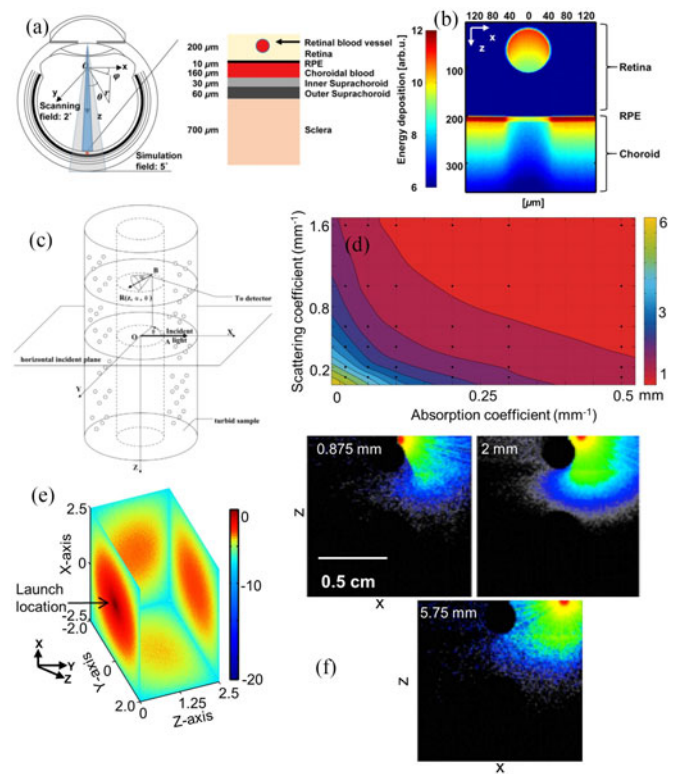

Fig. 2.   (a) Concentric spheres model for simulation of eye, with the details of posterior eye, (b) representative b-scan of energy deposition. Reproduced with permission from [23]. (c) Hollow cylinder for simulation of endoscopy imaging, (d) the contour plot of penetration depth for different optical properties for a circular probe of 1 mm radius. Reproduced with permission from [24]. (e) Raman photons from the inner cuboid across four planes of walled cuboid mimicking chemical concealed in a plastic container. Reproduced with permission from [25]. (f) Fluence for various drill-fiber distance for brain model in endonasal surgery. Reproduced with permission from [26].

2) Concentric Models of Regular Geometric Shapes: The applications of MCML grew widely beyond skin layers to light propagation in eye, endoscopy, and so on. Hence, the concept of MCML was extended to concentric spheres, concentric cylinders, and walled cuboid for more realistic approach [23]–[25], [29]. The simulation mediums were defined in spherical, cylindrical, and Cartesian co-ordinate system, respectively.

Fig. 2(a) and (b) are the eye model and its absorption distribution. Retinal imaging is important to monitor the melanin pigment in retina degradation, which leads to age-related and blindness disorder. PA ophthalmoscopy is used to capture retinal images. The proposed eye model was used to study the feasibility of PA signals to monitor the retinal blood vessels [23]. Eye ball constituted of six layers and the diameter was 23 mm. A cylindrical blood vessel along with its vessel wall (100 μm diameter) was placed 10 μm beneath the retinal surface. Spherical coordinate system was used to propagate the photons in this MC simulation. Light energy was recorded from 0° to 5° which is marked in Fig. 2(a). The absorbance along the simulation field is shown in Fig. 2(b). Melanin concentration was estimated by the ratio of energy deposited in the blood vessel and in the retinal pigment epithelium. The ratio varied between 2% and 9.5%

based on the melanin concentrations. The eye model which included the curvature of eye was used to study the change in PA signal amplitude due to the melanin concentrations in retina.

Concentric cylinders [see Fig. 2(c)] model was simulated for endoscopic surgery [24]. Effect of optical properties on the depth of penetration and the required source–detector distance was studied using this hollow cylinder model called endo-MCML. The simulation geometry was defined in cylindrical co-ordinate system, and both the source and detector were on the inner surface of the cylinder. The contour shown in Fig. 2(d) represents the optimal distance between the source and the detector for the given optical properties of the tissue being imaged. Endo-MCML results for esophagus model showed that to detect diffuse reflected light from deep tissue, larger source–detector distance needs to be used.

MCML was modified to simulate walled cuboid model to validate the Raman experiment, where chemical sample was filled in a cuboid container [25]. Six planes of the inner cuboid and the six planes of the outer cuboid were defined by plane equation. Raman photons transmitted from the outer cuboid were recorded along with the label of the layer in which they were converted to Raman. The MC code was modified to generate Raman photons at a probability of 10^{-6}. Raman photons detected from the sample (inner cuboid) along the four sides of the outer cuboid are shown in Fig. 2(e). From the visualized cuboid it was concluded that Raman signal from material can be detected at any of the six planes.

B. Irregular-Shaped Simulation Medium

The layered model or the double-concentric sphere model of the brain was very simplistic and unrealistic [30]. The planar geometry of MCML was replaced by regular prisms of infinite height in z-axis, to simulate 2-D human brain [31]. Complex mouse optical simulation environment (MOSE) was developed to track photons in a mouse model for bioluminescent imaging [14], [32]. Ellipsoids, cylinders, and polyhedrons were the building blocks of MOSE. Structural MRI images of human brain were segmented into voxels, each voxel was assigned optical properties of the tissue it represented, and photons were tracked along these voxels [33]. Whereas, in TIM-OS and MMC, the MRI images were converted to meshes for tracking of photons. Voxels or the mesh elements are assigned the optical properties of the medium in which they lie.

1) Voxel-Based Geometry: The tissue geometry was represented as a 3-D matrix of voxels (also called as parallelepipeds), which were of uniform size [34]. The optical properties of the medium were stored in a structure and the voxels were assigned positive integers representing the tissue type. Photon was tracked from voxel to voxel [10]. Note that the absorbance and scattering of photons in vMC was the same as MCML. Step-size of the photon computed at each scattering site in the vMC was computed as $p_s(s) = (\mu_a + \mu_s)e^{-(\mu_a + \mu_s)s}$. Pseudo-random numbers were obtained using Marsaglia's "subtract with borrow algorithm" which was available in MATLAB [35]. To avoid boundary condition check at each voxel, voxel library was constructed with the optical properties of the tissue assigned to

the voxel, which also accelerated the photon tracking [36]. vMC for skin and brain are discussed further.

When the number of blood vessels in the skin increased, the simulation geometry was modified to vMC [37]. Nine blood vessels were embedded in skin. Checking for interaction of photon with the cylinders using parametric equation at each scattering site is computationally expensive. Hence, a 3-D matrix was generated with optical properties assigned to each voxel. This model was used to study the heat propagation during port-wine stain treatment. Simulations suggested that pulse duration greater than 6 ms leads to injury of small-range blood vessels. The other 3-D models designed in voxel MC were brain and prostate gland [38], [39].

PAI was essential during endonasal surgery to ensure that the drill tool does not puncture the arteries of the brain [26]. Hence, the path of drill tool, skull, and the brain tissue with embedded arteries, was developed. Simulation geometry for PAI of endonasal surgery was converted to voxels to perform the MC. Illumination source was a fiber tip. Optical properties of drilling tool, brain, skull, artery, and air were assigned to the respective voxels. Spherical drill tip had a diameter of 2.9 mm. Fluence maps obtained for different tool to fiber distances [see Fig. 2(f)] were studied. Fibers too close to the drill shaft were not preferable, because the shaft blocked maximum light. The arteries were poorly illuminated when the fiber was far from the shaft. Optimal fiber–drill distance was identified as 2.4 mm.

2) Mesh-Based MC: Finer voxels were required when higher accuracy in absorbance distribution was needed [35]. Increased number of voxels increases the computation time. Triangular MMC was proposed by Ren *et al.* and tetrahedron-dependent MMC was developed by Fang *et al.* to handle the simulations which require irregular-shaped medium such as rat brain, adult brain, and neonatal brain [14], [31], [40]–[49]. MOSE is MC simulations, where multiple objects are embedded in a medium, which is used to model mouse for fluorescence tomography and bioluminescent tomography [14]. The region of simulation is converted to triangular meshes. The light source (such as fluorophores) is defined within the simulation medium. This photon launch from within the medium was not incorporated in the other MC techniques. Trabecular bone was also modeled by converting CT images into triangular meshes [49]. Each triangular mesh element was assigned with the optical properties of the medium, which lies on its surface normal. Meshes generated using MATLAB-based iso2mesh toolbox were defined by the nodes and each mesh was indexed (numbered).

Face-neighbor list was precomputed for each mesh element. Absorbance and scattering of photons in each mesh element was done in a similar manner as described for MCML. Plucker co-ordinate system was used for ray (photon)-polygon (mesh face) interaction. Energy deposition (absorbance) of photons was recorded using Barycentric co-ordinate system. The mid-point between the current and the next location of the photon is calculated and the node enclosing the mid-point accumulates the energy.

Preterm infants MRI scans were converted to meshes for simulations of DOT. These 4-D images were required for image reconstruction on accurate, age-matched anatomy. Meshes were
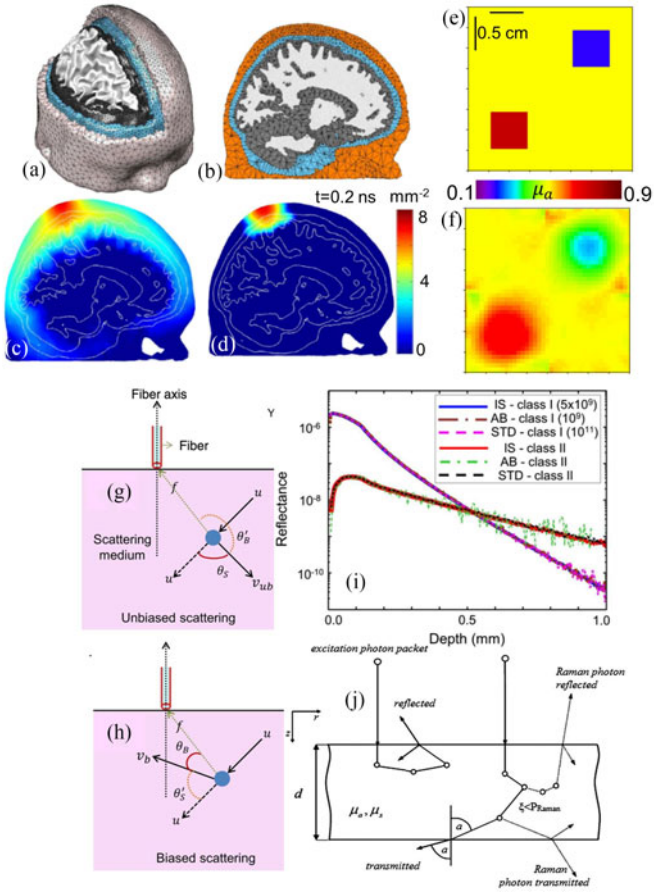
Fig. 3. (a) 3-D structure of adult brain, (b) sagittal-cut of the finite element mesh, (c) continuous fluence, and (d) time resolved at $t = 0.2$ ns. Reproduced with permission from [31]. (e)–(f) Real and reconstructed distribution of flux recording. Reproduced with permission from [50]. (g)–(h) Biased and unbiased time-domain optical coherence tomography. (i) Class I and class II photons detected from single-layer tissue. Reproduced with permission from [51]. (j) Two different photon propagation techniques for Raman scattering. Reproduced with permission from [52].

generated for gray matter, white matter, and the skull. Maximum mesh size was 1 mm³. About 345 detectors were distributed on the cranium. Log plot of the sensitivity profile along A/Ar plane were examined [46]. These simulated images for preterm to term newborns allowed age-matched and anatomically meaningful reconstruction of DOT images. In another simulation for time-resolved NIRS, 3-D brain model of adult brain was generated [see Fig. 3(a)]. Meshes were generated for scalp, CSF, gray matter, and white matter. They were smoothed using the Laplacian algorithm. Denser meshes were generated close to the complex cortex surface. Point source illumination was positioned at the center of the head. Fig. 3(b) is the sagittal slice of the brain for which the initial fluence distribution [see Fig. 3(c)] and fluence distribution at 0.2 ns is shown [see Fig. 3(d)].

IV. LIGHT ILLUMINATIONS

Many applications require simulations to optimize the light delivery. Pencil beam (point source) light illumination used in MCML is too simple and unrealistic since such light sources

are not easily available in practice. Absorbance, transmission, or reflectance estimated for a point source by MCML was theoretically convolved (CONV) for other illumination sources, such as Gaussian beam, top hat source, and circular beam [53]. Convolution, of course assumes that the system is linear and shift invariant. CONV cannot be used when this condition is not satisfied. Below several common light illumination schemes for shift variant models are discussed in detail.

In many applications, the light launch location can be at multiple locations and with different angles as well. In one of the studies, where the light delivery was optimized for PAI, MCML was modified to incorporate various light launching situations in an embedded sphere model [27]. The launch locations of the photons were around the ultrasound transducer for more realistic optimization of illumination angle [27]. Point source at the center (origin) was compared with sources split across the minor axis of the transducer, major axis, and ten sources were distributed along the face of the transducer. Even though the absorbance in sphere was high for illumination from origin, practically it is rather a challenging task to deliver the light through the center of the ultrasound probe. Hence, the design of point sources across the minor axis of the transducers was chosen.

The closest (to pencil beam) light illumination one can achieve is the light launch using a fiber. The radial distribution of the photon from the fiber tip (for many applications the fiber tip is also approximated as a point) and the angular orientation of the photon due to the numerical aperture (NA) of the fiber were simulated [54]. Simulation of photon launch from the fiber tip was used to optimize the source–detector position. Illumination from fiber bundle at an angle was also simulated to study the effects of change in angle on the absorbance in imaging of sentinel lymph node modeled as sphere [55]. The fiber bundle consisted of multiple multimode fibers randomly packed inside the bundle. Illumination at an angle of 15° was optimum when the sphere was on surface (0.5 cm), but the angle of illumination had lesser effect on spheres at the depth of 3 cm. In another study discussed earlier (see Section III-A2), angular beam of 2° from fiber tip was the illumination source [23].

For microscopic applications the light was launched through lens which focusses the light to a diffraction-limited spot. Diffraction of photons is ignored in traditional MC, because the wave nature of photon is not considered. Hence, in the simulations of Gaussian beam illumination, the launched photons focused at a point in the medium which was undesirable. To overcome the shortcoming, the Gaussian beam profile formed by the lens was simulated during the launch of the photons to focus at the diffraction-limited focal spot [56], [57]. This was achieved by propagating the unscattered, ballistic photons along the curved trajectories predicted by Gaussian optics. The Gaussian beam was focused by a lens of NA 0.2 at focal distance of 0.8 mm (in air) [56]. The proposed model was capable of handling mismatched refractive index between layers. Better modeling of Gaussian beam illumination increased the accuracy in estimation of fluence distribution within focal depth.

Meshes of object of interest (whole rat or human brain) were combined (restessellated) with the meshes of source and

detector [40]. A single (red) tetrahedron enclosed the source which was merged with the mesh of Digimouse. Tessellation done in the preprocessing step reduced the computational cost, since the numbers of nodes were reduced. The results of wide field illumination implemented in MMC were compared with that of vMC. The fluence distribution in both of the algorithms was spatially and temporally identical.

V. INTERACTION OF THE PHOTON WITH THE MEDIUM

Once a photon is launched on the medium (or inside the medium), the photons are tracked inside the medium. Conventional MC was sufficient for simulations of few imaging modalities such as NIRS, DOT (which depends on diffuse-reflected photons), and PAI (which depends on absorbance). Nonetheless, the straightforward tracking was modified to simulate other optical imaging techniques, such as OCT, Raman imaging, terahertz imaging, and polarization imaging, which are discussed here.

A. Frequency Domain Optical Tomography

MCML was modified for simulation of frequency domain optical tomography [50]. Based on the modulation of the signal (cosine or sine), the photons' weight was either real or imaginary. Time-domain source at a given position, in a particular direction and at a given time, was converted to frequency domain using the Fourier transformation. Once initialized in the frequency domain the photons moved to the scattering site as seen in the MCML but the weight dropped by the photon was with respect to its phase. The imaginary weight dropped by the photon at the ith step was given by $\tilde{W}_i \times e^{\left(-\frac{i\omega}{c}s_i\right)}$, where $\tilde{W}_i$ was the current weight of the photon, c is the speed of the light, ω is the frequency of modulation, and s_i is the step size taken. Both the real and the imaginary weight of the photon were reduced. This forward frequency domain MC was used along with the perturbation MC to determine the optical properties of the medium. Fig. 3(e) is the distribution of the absorption coefficient that is the input for which Fig. 3(f) is the reconstructed distribution.

B. Optical Coherence Tomography

OCT is an imaging modality which depends on the backscattered photons. Since the biological medium are highly forward scattering, the number and strength of backscattered photons are less. Hence, simulations for OCT require tracking of large number of photons to ensure the statistical significance of the photons detected at the collecting optics [51], [58]–[61]. Simulation of increased number of photons increases the computation time. To achieve statistically significant results in reduced simulation time, probabilistic approach was used to bias the photons towards the collecting optics. Probability of the photons reaching the collecting optics from the probing depth was increased by biasing the scattering angle of the photon toward the collecting optics [61]. The probability of polar angle sampled using HG function, $p(\cos\theta)$ was used to calculate $-\cos\theta$ for angular biasing of the photon. In order to maintain the statistical validity, the weight of the photon was adjusted by the proportion $\frac{p(\cos\theta)}{p(-\cos\theta)}$. Since the photons were biased to the collecting optics only when they reached the probing depth, simulations had to be run for each probing depth (simulation time ~42 h). Hence, a more computationally efficient importance sampling (IS) technique was developed.

IS is another probabilistic method for biasing the photon toward collecting optics. The biased and unbiased scattering is shown in Fig. 3(g) and (h). The site of first biased scattering was randomly chosen. Hence, biasing of photons to the collecting optics using the IS technique was independent of probing depth. During a biased scattering, the direction cosines of photon were updated using modified HG, which is as follows:

$$p\left(\cos\theta_B\right) = \left(1 - \frac{1-a}{\sqrt{(a^2+1)}}\right)^{-1} \times \frac{a\left(1-a\right)}{\left(1+a^2-2a\cos\theta_B\right)^{\frac{3}{2}}} \tag{1}$$

where a is the bias coefficient. The weight of the photon in the IS technique was compensated while recording based on the likelihood ratio of a biased and an unbiased scattering. The improved IS algorithm was validated across standard MC [see Fig. 3(i)] [51]. The IS-based speeded-up MCML-OCT was executed for embedded objects. Simulations for B-scans (which had 50 A-lines) of the embedded objects took 54–110 h.

C. Raman Simulation

Raman imaging was also simulated using MC [25], [52], [62], [63]. At each scattering site, a random number was generated and compared to Raman probability (defined by user) to decide if the current photon should be converted to Raman photon [Fig. 3(j)]. This conventional Raman photon generation was compared with one more Raman photon generation technique. In the second method, Raman photons were generated from each scattering site and isotropically relaunched for propagation [52]. The second method (relaunching from each scattering site) had better statistical significance compared to the direct method (conversion of the photon into Raman with respect to random number). Conventional Raman photon generation technique with Raman probability of 10^{-6} was used in the previously discussed example of Raman photon detected from the material sealed in a plastic container [see Fig. 2(e)]. In another work, nonlinear MC was implemented for execution of simulated Raman scattering [62]. The launch of the photons was time gated. Time taken by the photons during scattering events was also tracked for synchronization. Modifications were done to handle the Raman scattering and the simulated Raman scattering. Experimentally, the Raman scattering is 5–10 orders of magnitude smaller than Rayleigh scattering. Hence, one needs to simulate MC for large number of photons ($\sim 10^8$) which is time consuming.

D. Polarization of Light

In most of the conventional simulations, the polarization of the light was ignored. However, the polarization of the light can also be considered when needed. During the launch of the photons, polarized light propagation was done by defining the
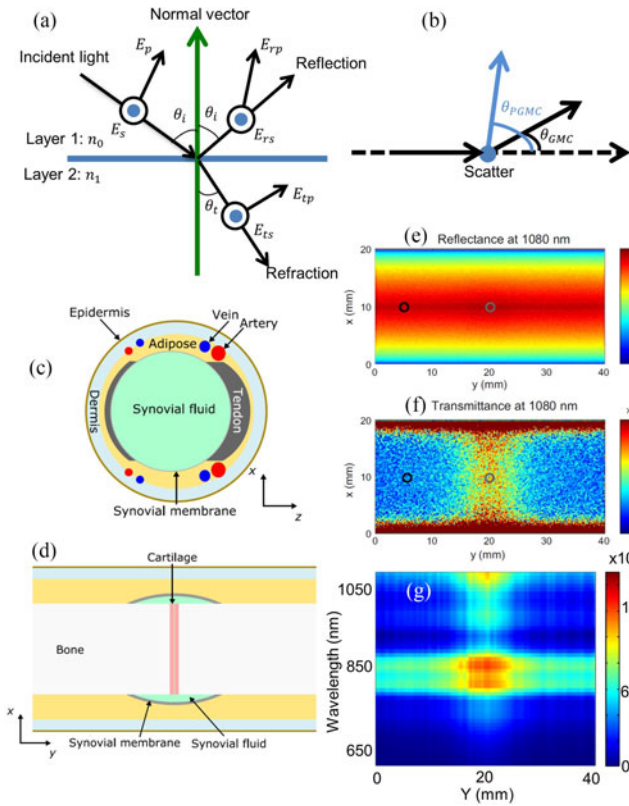
Fig. 4. (a)–(b) Reflection and refraction for simulation of polarization imaging. Reproduced with permission from [64] and [65]. (c)–(d) Cross section of the joint in *xz* plane and *xy* plane, (e)–(f) reflectance and transmittance at 1080 nm, (g) transmittance spectrum along the finger axis. Reproduced with permission from [66].

Muller matrix which was updated at each scattering, refraction, or reflection event [65], [67]. Muller matrix was formed by the Stokes vector which describes the polarization state of light. Scattering particles were assumed to be of comparable diameters with respect to wavelength; hence, Muller matrix was derived using the Mie theory. Initial Stokes vector and the corresponding Lagrangian coordinate frame was specified during the photon launch, where Lagrangian coordinate system of photon includes parallel electric field vector, perpendicular electric field vector, and the direction cosine vector which were orthogonal [see Fig. 4(a)]. Absorbance was similar to standard MCML, but the scattering was from intensity function derived from the Mie theory (instead of HG function) as shown in Fig. 4(b). Once the photon hits a launch surface after propagating through the medium, the detection of the photon was with respect to the Lagrangian coordinate frame which undergoes four rotations (two azimuthal rotations and two scattering rotations). Polarization-sensitive MC was useful to understand the effect of polarization on laser energy deposition.

E. Other Imaging

Terahertz (THz) imaging was also simulated using MC [68]–[71]. The photon distribution along the THz spectrum is based on statistical sampling. Seven-layer skin model along with blood vessels were modeled for comprehensive polarization and THz simulation. Note that inside the simulation medium many cells were incorporated as cuboid shape. In another example of THz imaging of skin with nanoparticles, skin was modeled as four layers [69]. Polarization state of the photon was recorded at each scattering site. Muller matrix was determined by the scattering, absorption, and rotation of the photon to and from the reference planes. This matrix determines the Stokes vector relationship between the pencil beam and the reflected photon. The simulation of polarization and THz for skin was required to understand the sensitivity of these imaging techniques to change in water content.

Conventional MC was simulated for optical properties of tissue at different wavelengths to simulate hyperspectral imaging (HSI) [66]. HSI was simulated for estimation of reflectance and transmission of normal human finger joint and rheumatoid arthritis joints. Three-dimensional finger models were developed with the help CT and MRI images. Suitable optical properties were assigned to the regions (epidermis, dermis, blood vessel, synovial fluid, and tendon) for optical range of 600–1100 nm. Fig. 4(c) and (d) is the model and Fig. 4(e) and (f) are the reflectance and transmission at 1080 nm. Transmission for different wavelengths along the *y*-axis is shown in Fig. 4(g). From the simulations, it was concluded that transmission images can be used to detect arthritis.

The scattering of the conventional MCML was modified for diffuse photon density wave (DPDW) imaging [72]. DPDW is the frequency domain method, where the dynamic response of the scattered light intensity to the modulation of incident laser beams intensity is from 50 to 1000 MHz. This frequency domain imaging was immune to noise. The scattering and absorbance was done in frequency domain. Conventionally, photon migration was done in time-domain and its Fourier transform was taken for simulation of frequency-domain imaging systems [73]. In the approach proposed by Kuzmin *et al.* all the launched photons contributed to the detected signal. Moreover, the Bethe–Salpeter equation was solved instead of solving the RTE at microscopic level to compute the scattering intensity. Results of modified MC were compared with experimental results of intralipid suspensions of various concentrations.

MMC was also modified for fluorescence imaging [47], [74], [75]. MC was modified with weighted direct emission for generation of fluorescence photons. Excited photons and the fluorescence photons were tracked with different optical properties. Similar to Raman photon generation, the first scattering of the generated fluorescence photon was isotropic scattering. The CT scans [see Fig. 5(a)] were converted to voxels or meshes [see Fig. 5(b)]. vMC and MMC were performed for fluorescence. Fig. 5(c) is the fluorescence image of the whole kidney. Fig. 5(d) is the five slices of fluorescence simulation. In another study. CT scans of human head were converted to meshes to simulate NIR imaging of sinus. Fig. 5(e) is the photon count overlaid on the CT slice shown in Fig. 5(f). Fig. 5(g) is the photon count for different illumination patterns [45]. Patient CT slices were used for simulation and simulation results were compared with measured NIR. From simulations, it was observed that the illumination at the center of the palate significantly reduced the image quality.
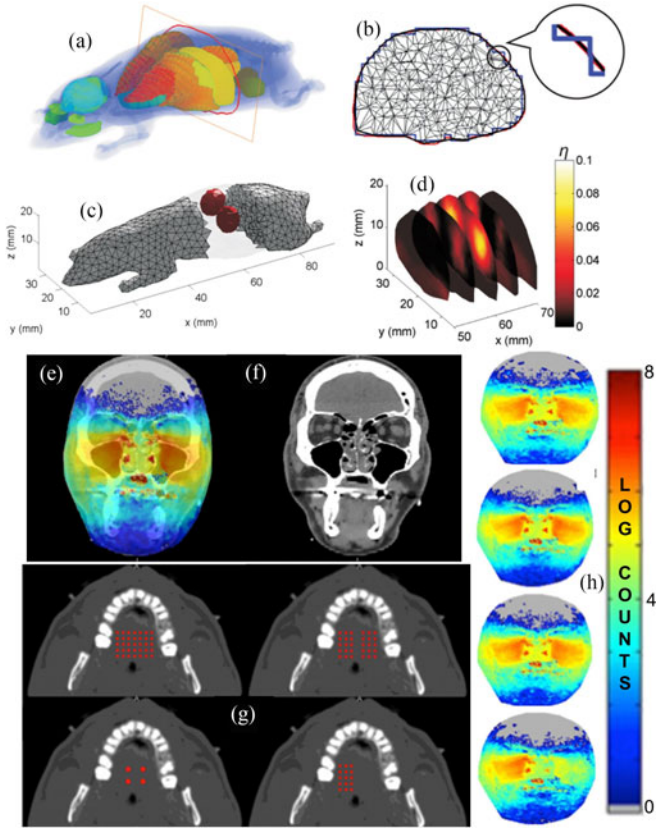
Fig. 5. (a) High-resolution mouse atlas, (b) boundary approximation for mesh, (c) volume reconstructed from simulated fluorescence slices, (d) selected five slices from $x = 50$ to 70 mm. Reproduced with permission from [47]. (e) CT slice of head shown in (f) with the number of photons reaching the NIR sensor. (g) Four different illumination profile. (h) Photon count for various illumination profile. Reproduced with permission from [45].

VI. REFRACTION

To simulate the roughness of the refractive surface (mainly observed in metallic surfaces), the refractive surface were divided into small microfacets [64]. In one of the applications, two layers of microfacets reflected and refracted light specularly. The area of each microfacet was much larger than the wavelength. Normal vector in $x-$ and $y-$ direction for each microfacet was randomly distributed. The model was incorporated with polarization and compared with analytical bidirectional reflection distribution function model. The angle of polarization, degree of polarization, and the four Stokes vector from single-layered copper with roughness parameter 15 μm were studied.

Another example of rough surface compensation is seen in simulation of back scattering of coherent linearly polarized light from tissue [76]. Electric field MC was introduced by Doronin *et al.*, which considered the laser speckle and depolarization of the linearly polarized light back scattered from the tissue due to surface roughness. Jones formalism was used to handle circular and linear polarization. Polarization vector $\vec{P}_i$ was updated at each scattering site. The state of polarization is $\vec{P}_i = -\vec{e}_i \times [\vec{e}_i \times \vec{P}_i]$, where $\vec{e}_i$ is the unit vector along the direction of propagation after the $(i-1)th$ scattering event. Along

with electric field modeling for change in polarization, phase shifts due to the roughness were taken into account. CUDA and graphical processing unit (GPU) were used to speed up the light propagation. Simulation with 10^{11} photons took approximately 2 h [76]. The roughness parameter was varied from 0 to 65.8 μm. The model was validated through phantom study.

VII. RECORDING OF THE PHOTONS

MC output was modified to record the photons that travel in hemispherical- and axicon-shaped lensed fiber [77]. Twofold increase was seen in signal collection with the lens compared to bare fiber tips. With advancement in the applications of MCML in various imaging techniques, the recordings of photons also varied. In simulations of OCT, only the photons that reach the collecting optics (which is specified by the diameter and acceptance angle of fiber) were recorded [51]. The photons that reached the probing depth were recorded as Class I photons, which was the signal, and the photons that had not reached the probing depth were recorded as Class II photons, which contributed to the noise [see Fig. 3(l)]. For simulations of Raman imaging, conventionally the depth at which the photon was converted to Raman was recorded. In one of the simulations which focused on the layer in which the photon was converted to Raman, the photons were tagged with the layer index [23]. Fig. 2(e) is the reflected or transmitted photons that were converted to Raman in the material. For polarization imaging, the four Stokes vector (which are initialized to [1, 0, 0, 0]) were updated throughout the propagation and recorded independently once the photons were killed [64]. Photons were tracked in Digimouse model and recorded till they reached the square detectors which mimicked charge coupled devices (CCD) [40].

MC for a medium with low optical properties remained a challenge. When the absorption and scattering coefficients of the medium is very low, the efficiency of MCML drops, since the number of steps taken by the photons in the finite medium reduces. In such situations instead of calculating the photons weight drop at a particular location, the fluence was estimated. In one example, the MMC was modified to compute flux of the photon, where the absorption coefficient of the mediums were 0.004 and 0.1 mm^{-1} and scattering coefficients were 0.01 to 45 mm^{-1} which are very low [41]. Note that the illumination here was through fiber source (NA is 0.39 and diameter is 200 μm). Once the photon was launched, the propagation distance was computed using $l_a = -\ln(\xi)/\mu_a$, which was governed only by the absorption coefficient hence decoupling from scattering coefficient. The number of photons entering each mesh element was recorded as flux. The fast TIM-OS algorithm was used to find the next intersection mesh. The intensity map obtained from photon flux recording algorithm and the intensity map by conventional weight loss algorithm were compared. Photon flux distribution in a low scattering domain such as cerebral fluid was used to study the light distribution in the neural target (with optogenetics toolbox) when the illumination source is a fiber.

Perturbation MC is another application where recording of the photons is crucial [79]–[81]. It was used to estimate the

TABLE I
COMPARISON OF TIME TAKEN FOR A GIVEN SIMULATION GEOMETRY BY
DESKTOP AND GPU [83]

	Time (s)	Power (W)	Photons/Joules
Core i7 (Seq. MCML)	577	20	867
Core i7 (four threads)	52	70	2747
Core i7 (eight threads)	40	110	2247
GTS	9	95	11 103
Statix V	27	13	28 490

optical properties of an unknown medium. The prediction is done in two steps—baseline and estimation. In the baseline, simulations were run for a medium whose optical properties are known. The weight of the photon, path traced by it and the number of collisions encountered were recorded during the exit (as reflectance or transmittance). Perturbation theory is used to estimate the relationship between the new tissue properties and baseline tissue properties. The accuracy of determination of optical properties depends on the closeness of the baseline properties to it since perturbation is an approximation. It is used due to its simplicity and speed. This technique is widely applied for estimation of skin properties.

VIII. OPTIMIZATION OF THE MC CODE

Computational resources limited the use of MC in many cases due to the heavy computational burden. Hence, the focus of MC users was to increase its speed. Liu and Ramanujam developed a scaling method to estimate diffuse reflectance for a range of optical properties from a single simulation [82]. Apart from run time improvement by probabilistic approach, computational efficiency was also improved using GPU which were dependent on CUDA programming [14], [48], [83]. With advancement in high-speed computers the computational time has significantly decreased today compared to the time when MC was introduced. However, for simulations involving large simulation volume, such as human brain, the computation expense still remains high due to the memory requirement. Computation speed was improved by using either faster hardware or by using smart algorithm to reduce the number of the photons that needs to be run.

Multiple runs of MCML were executed on clusters which enabled parallelization of runs [25]. For better performance, individual photons were tracked in parallel. With use of field-programmable gate arrays and GPU, 21x and 64x speed enhancement was reported for platforms such as core i7, GTS 450, and stratix V, which is shown in Table I for conventional multi-layer model [78], [84]–[87]. GPU was also used in speeding up the mesh-based simulations [78]. The human head model was segmented into skin, skull, and brain [see Fig. 6(a)–(c)] and photons were tracked with respective optical properties at 900 nm for simulation of NIRS imaging. Optimization was done to reduce the memory usage by saving the photon trajectory nodes as array of grid co-ordinates as opposed to saving them as grid cells. The threads were synchronized for GPU. The ray–polygon intersection search was assisted by bounding volume hierarchy tree search to utilize the hardware cache better. Fig. 6(d) is the
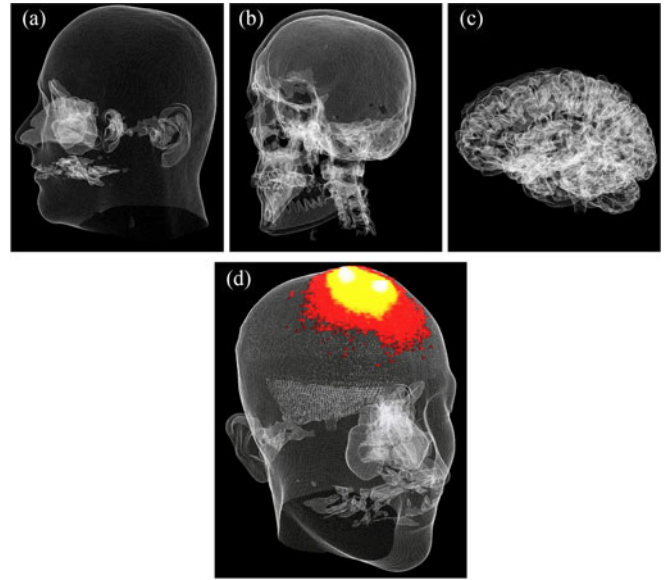

Fig. 6. Light propagation in head model for near-infrared spectroscopy, (a) skin, (b) skull, and (c) gray matter, (d) 3-D photon trajectory map at a source–detector distance of 4 cm and a wavelength of 900 nm. Reproduced with permission from [78].

photon trajectory map for source–detector distance of 40 mm. Use of GPU increases the speed by 11 times compared to single thread CPU.

OCT MC was speeded up through CUDA and probabilistic approach (improved IS) [88]. CUDA simulation took 2.9 min which was one order of magnitude less than conventional MCML which took 43 min. OCT simulations of standard MCML (for 10^{11} photons), angle biased MC (for 10^9 photons), and IS (for 5×10^9 photons) were implemented for homogeneous medium to compare simulation time [see Fig. 3(l)]. Even though the intensity predicted by the algorithms were identical across depth, angle biased approach took half the time taken by MCML, whereas IS-based approach took 6 h which was one-fifth the time taken by conventional MCML.

IX. APPLICATIONS OF MC SIMULATIONS

MC is widely used for skin modeling [89]–[91]. Experimental and simulated OCT images of skin were used to see the effect of thickness of epidermis [92]. In another work, oxygen saturation in skin was studied using MC [93]. Forearm was modeled as three-layered tissue model along with radial artery located at 6 mm below the skin [94]. MC of skin with absorbers such as melanosomes were modeled to predict the reflectance of hyperspectral light from 250 to 2500 nm which comprehensively represented the spectral and spatial distributions of light [95]. Effect of different illumination pattern for PAI of melanoma studied using MC was essential for bedside treatment planning [96].

To know the volume of tissue imaged by the fiber in the brain, MCML simulations were run with optical properties varying with respect to oxygen saturation [97]. MC simulations were done with AtlasViewer software to study the range of fluence distribution in brain tissue [98]. Adult brain simulations were

carried out to ensure delivery of light in the desired region of brain with different probe placement combinations in far-infrared imaging [96].

Light delivery through transvaginal probe and transurethral probe was studied for treatment of female stress urinary inconsistence [99]. The absorbance map obtained from MC was converted to heat map based on Arrhenius integral thermal damage calculations. Simulations showed that transvaginal approach was better than transurethral approach because 37% of energy was absorbed in endopelvic fascia in transvaginal case, whereas only 18% of the energy was deposited in the secondary approach. Transvaginal probe was also exploited for real-time ovarian imaging [100]. Similarly, transurethral and transrectal probe designs were explored for PA endoscopy of prostate cancer [101], [102]. Adipose tissue, urethra wall, rectum, and prostrate with tumor were included in the model which was defined by voxels. Light source of 763 nm was placed either in urethra or in rectum. These simulation studies clarified that transurethral configuration of light delivery was optimum. Light propagation through a semi-infinite layer of human mucosa tissue was simulated to study the fluence distribution from a diverging laser source [103]. This simulation was done to study the absorbance distribution for PA esophageal endoscopy.

Other than these, there are many other areas of application of the MC simulations. Some of them are listed below.

1) To study the advantage and disadvantage of confocal and anticonfocal microscopy for middle ear imaging, MATLAB-based MC was used with light focusing through a lens [105].
2) Detection of iron deficiency from lips [74]. Anticonfocal system was seen to perform better in terms of background rejection.
3) MC simulations for OCT images of human tooth was experimentally validated [106].
4) Geometry and tracking (GEANT4)-based MC simulations of eye were also done to study the reflected beam profile from retina [107]. Recovering the absorption and scattering coefficient of the medium is essential to categorize it as normal tissue or as tumor.
5) Inverse MC was used in DRS to compute the optical properties of the medium [108].
6) PAI was used for early detection of prostate cancer for which MC was used to design light delivery [38].
7) Optical properties were varied over time in a time-gated MC for modeling of Doppler flow [109]–[111].
8) PA wave was modeled from the absorbance obtained from vMC simulations [112].
9) NIRS of sinus was simulated using MMC to study the light delivery [44].
10) Simulation of new-born infants lungs was done to monitor gas volume through laser spectroscopy [113].

X. Discussions

The simulation geometry for MC was defined by parametric equations (pMC) or voxels which is vMC or as tetrahedrons in
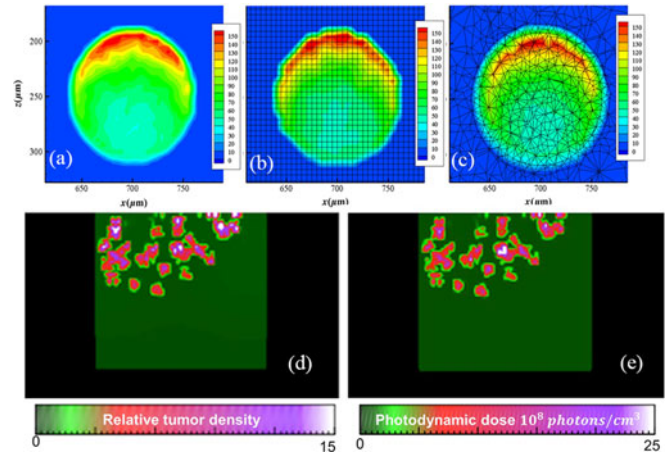

Fig. 7. Absorption along the plane of sphere center: (a) Geometric MC, (b) voxel-based MC, and (c) mesh-based MC for an embedded sphere to study the effect of different simulation set-up. Reproduced with permission from [104]. (d) Simulation geometry with tumor modeled as fractals, (e) absorbance across the tumor. Reproduced with permission from [89].

MMC [13], [104], [114]–[116]. Two-layer skin model with a blood vessel was modeled to study the accuracy of the three geometries [104]. In parametric domain, the boundaries were determined by equations of cylinder and planes, in vMC, the cylinder boundary was approximated to 5 μm cubic voxels, and for MMC tetrahedral meshes of maximum 10 μm were generated. Fig. 7(a)–(c) is the photon deposition in pMC, vMC, and MMC. pMC had the least error at the boundary of blood vessel. MMC needed local refinement at the boundary for better handling of curved boundaries. Another study was done to compare the effect of discretization when blood vessels were approximated to the Cartesian co-ordinate system (vMC) and the analytical tracking of photon (pMC) [117]. vMC results varied erratically with the voxel size. pMC was 25 times faster than vMC. Effect of number of photons on error in deposition and distribution of absorbance was studied [28]. Error in energy deposited was 0.1% for number of photons more than 10^6. However, distribution error was less than 10% only when 1.2×10^7 and 2.2×10^7 photons were run for pMC and vMC, respectively. Blood vessels along with skin were modeled as voxels. The optimal number of voxels and the number of photons required were experimented. The light deposition along the laser-spot center for varying number of photons when voxel size was 20 and 5 μm, was studied. The voxel size depends on the diameter of the embedded blood vessel and the optical properties of the medium [10]. The grid size (Δw) for a blood vessel of diameter (d) is given by $\Delta w \mu_t = 0.1 d \mu_t$ when $d \mu_t \leq 2$ and $\Delta w \mu_t = 0.2$ otherwise, where $\mu_t = \mu_a + \mu_s$. It was concluded that one needs to run the simulation with number of photons at least five times the total number of voxels.

One more comparison was done between mesh-based and two-layer-based MC for light propagation in brain [118]. These two models performed better than the homogeneous (single layered) brain model used conventionally. Nonhomogeneous medium such as tumor with different cell density was modeled as fractals by Campbell et al. [89]. The fractal model was used

to mimic the nonuniform structure of a cylindrical tumor. The mass of the tumor was clustered and fractals were used to form the 3-D structure. The 3-D nonuniform structure was pinned to voxels for MC simulation. Sample tumor structure is shown in Fig. 7(d), and the absorption distribution is shown in Fig. 7(e).

MCML is widely used for its simplicity of defining the medium as planes (for example skin) and therefore it does not need CT/MR structural images. Ignoring the curved boundaries is a disadvantage of MCML. Nonetheless, one can use this model only for preliminary studies, where approximate measurements of diffuse reflectance, diffuse transmittance, or absorbance are satisfactory. Due to the simple equations used to detect boundary crossing, the time taken by MCML simulations on desktop is less compared to vMC and MMC. MCEO is ideal for simulation of phantom studies, where the medium can be defined by parametric equations. Definition by parametric equations is not sufficient for representation of complex human or small animal anatomy. Time taken by MCEO is also less than vMC and MMC. vMC converts the 3-D CT/MR structural volumetric data into voxels. There is a loss of accuracy at the boundaries of organs/tissue layers due to the approximation as voxels. The time taken by vMC is reduced with the help of voxel library. After the introduction of iso2mesh toolbox in computational geometry algorithms toolbox, the organ boundaries are preserved, since MMC segments the CT/MR images of complex structures (human or small animal anatomy) into meshes. The computation time is high for MMC due to the boundary check at each mesh element.

The number of photons needed to run for MC simulation is an important parameter to consider [119]. Recently, a formula was derived to determine the number of photons required for convergence of the solution. However, this formula is valid when one is interested in calculating the diffused transmittance. When lesser number of photons was tracked, there was an energy sag in the middle point (origin) compared to the adjacent point. Henceforth $f(nn) = 0.1699 \times \mu_a + 1.0981 \times d - \frac{\ln\left(\frac{0.2}{0.6681 \times \mu_s + 15.5771}\right)}{0.9395}$ where 10^{nn} is the number of photons, d is the thickness of tissue, can be used to determine the number of photons for applications interested in the forward transmission of the photons.

Sassaroli and Martelli compared four different light propagating techniques which are Albedo-weight method, Albedo-rejection method, microscopic Beer–Lambert method, and absorption-scattering path length rejection [120]. The statistical equivalence of four methods was compared with respect to time-resolved reflectance. Validation was done across various source–detector distances. The discrepancies among the four techniques were within the standard deviation.

MC was also combined with other modeling tools due to its flexibility. GEANT is an object-oriented toolkit for particle propagation in matter. MC simulations were executed with GEANT4 architecture for medically oriented simulations [121]. MC was ported into MATLAB programming language for light propagation in optogenetics [122]. The 3-D mouse head atlas that existed in optogenetics software was combined with MC for light propagation in heterogeneous brain tissue [123].

Results or outputs of MC were widely postprocessed for additional information. A six-parameter equation was derived to use optical properties of tissue and beam radius to predict the light fluence by MC output [124]. Hence the user does not have to run the simulations for each beam radius. Absorbance maps (from vMC) were postprocessed to study the effect of rotating illumination in PA imaging of human breast [125]. Acoustic pressure data were generated for the MC simulations using spherical-voxel-based method which is detailed by Lou *et al.* [125]. Comparison was made between stationary and rotating illumination source based on the reconstructed images. It was concluded that to reduce the reconstruction artifacts, simple filtered back projection algorithm can be used for stationary illumination, whereas iterative reconstruction techniques were required for rotating illumination.

XI. CONCLUSION

MC simulation for light propagation in tissue is an important simulation tool to understand how light interacts with biological tissue for various applications. Although the basic principle of the MC simulations has not changed much over the decades, there have been significant improvements in terms of how different simulation geometries, various illumination situations, photon tissue interaction mechanism are incorporated for various applications. Note that the focus of the review is only in forward MC. Hybrid MC, where diffusion theory is combined with MC for speed enhancement is discussed in another review [126]. The applications of MC we discussed are mainly focused on biomedical optical imaging, however, there are other applications of MC as well [127], [128]. The future direction of MC simulations is to improve the simulation speed, use more anatomically realistic simulation geometry, and to develop a more user-friendly simulation tool box [129].

REFERENCES

[1] L. V. Wang and H.-I. Wu, *Biomedical Optics: Principles and Imaging.* Hoboken, NJ, USA: Wiley, 2009.

[2] S. H. Yun and S. J. Kwok, "Light in diagnosis, therapy and surgery," *Nature Biomed. Eng.*, vol. 1, 2017, Art. no. 0008.

[3] D. Wang *et al.*, "Deep-tissue photoacoustic imaging at 1064 nm using a contrast agent based on phosphorus phthalocyanine formulation," *Proc. SPIE*, vol. 10064, 2017, Art. no. 100642X.

[4] W.-F. Cheong, S. A. Prahl, and A. J. Welch, "A review of the optical properties of biological tissues," *IEEE J. Quantum Electron.*, vol. 26, no. 12, pp. 2166–85, Dec. 1990.

[5] P. K. Upputuri and M. Pramanik, "Recent advances toward preclinical and clinical translation of photoacoustic tomography: A review," *J. Biomed. Opt.*, vol. 22, 2017, Art. no. 041006.

[6] K. Liu *et al.*, "Evaluation of the simplified spherical harmonics approximation in bioluminescence tomography through heterogeneous mouse models," *Opt. Express*, vol. 18, pp. 20988–21002, 2010.

[7] B. C. Wilson, "A Monte Carlo model for the absorption and flux distributions of light in tissue," *Med. Phys.*, vol. 10, pp. 824–830, 1983.

[8] C. Zhu and Q. Liu, "Hybrid method for fast Monte Carlo simulation of diffuse reflectance from a multilayered tissue model with tumor-like heterogeneities," *J. Biomed. Opt.*, vol. 17, 2012, Art. no. 010501.

[9] L. V. Wang, S. L. Jacques, and L. Zheng, "MCML—Monte Carlo modeling of light transport in multi-layered tissues," *Comput. Methods Programs Biomed.*, vol. 47, pp. 131–146, 1995.

[10] D. Li, B. Chen, W. Y. Ran, G. X. Wang, and W. J. Wu, "Selection of voxel size and photon number in voxel-based Monte Carlo method: Criteria and applications," *J. Biomed. Opt.*, vol. 20, 2015, Art. no. 095014.

[11] A. Doronin and I. Meglinski, "Peer-to-peer Monte Carlo simulation of photon migration in topical applications of biomedical optics," *J. Biomed. Opt.*, vol. 17, Sep. 2012, Art. no. 090504.

[12] A. Doronin and I. Meglinski, "Online object oriented Monte Carlo computational tool for the needs of biomedical optics," *Biomed. Opt. Express*, vol. 2, pp. 2461–2469, 2011.

[13] H. Shen and G. Wang, "A tetrahedron-based inhomogeneous Monte Carlo optical simulator," *Phys. Med. Biol.*, vol. 55, pp. 947–962, 2010.

[14] N. Ren, J. Liang, X. Qu, J. Li, B. Lu, and J. Tian, "GPU-based Monte Carlo simulation for light propagation in complex heterogeneous tissues," *Opt. Express*, vol. 18, pp. 6811–23, 2010.

[15] C. Zhu and Q. Liu, "Review of Monte Carlo modeling of light transport in tissues," *J. Biomed. Opt.*, vol. 18, May 2013, Art. no. 050902.

[16] L. Wang and S. L. Jacques, "Animated simulation of light transport in tissues," *Proc. SPIE*, vol. 2134, 1994, Art. no. 2134A.

[17] V. Periyasamy and M. Pramanik, "Monte Carlo simulation of light transport in turbid medium with embedded object—Spherical, cylindrical, ellipsoidal, or cuboidal objects embedded within multilayered tissues," *J. Biomed. Opt.*, vol. 19, 2014, Art. no. 045003.

[18] S. A. Prahl, M. Keijzer, S. L. Jacques, and A. J. Welch, "A Monte Carlo model of light propagation in tissue," *Dosimetry Laser Radiation Med. Biol.*, vol. 5, pp. 102–111, 1989.

[19] Y. Liu, H. Wang, Y. Liu, W. Li, and Z. Qian, "Monte Carlo and phantom study in the brain edema models," *J. Innov. Opt. Health Sci.*, vol. 10, 2016, Art. no. 1650050.

[20] A. N. Bashkatov, E. A. Genina, V. V. Tuchin, G. B. Altshuler, and I. V. Yaroslavsky, "Monte Carlo study of skin optical clearing to enhance light penetration in the tissue: Implications for photodynamic therapy of acne vulgaris," *Proc. SPIE*, vol. 7022, 2007, Art. no. 702209.

[21] F. H. Mustafa, P. W. Jones, and A. L. McEwan, "Near infrared spectroscopy for body fat sensing in neonates: Quantitative analysis by GAMOS simulations," *Biomed. Eng. Online*, vol. 16, 2017, Art. no. 14.

[22] S.-C. Chung and C.-C. Sun, "Signal-enhancement reflective pulse oximeter with Fresnel lens," *Opt. Commun.*, vol. 375, pp. 9–14, 2016.

[23] X. Shu, W. Liu, and H. F. Zhang, "Monte Carlo investigation on quantifying the retinal pigment epithelium melanin concentration by photoacoustic ophthalmoscopy," *J. Biomed. Opt.*, vol. 20, 2015, Art. no. 106005.

[24] Y. Zhang, J. Zhu, W. Cui, W. Nie, J. Li, and Z. Xu, "Monte Carlo analysis on probe performance for endoscopic diffuse optical spectroscopy of tubular organ," *Opt. Commun.*, vol. 339, pp. 129–136, 2015.

[25] V. Periyasamy, S. Sil, G. Dhal, F. Ariese, S. Umapathy, and M. Pramanik, "Experimentally validated Raman Monte Carlo simulation for a cuboid object to obtain Raman spectroscopic signatures for hidden material," *J. Raman Spectrosc.*, vol. 46, pp. 669–676, 2015.

[26] B. Eddins and M. A. L. Bell, "Design of a multifiber light delivery system for photoacoustic-guided surgery," *J. Biomed. Opt.*, vol. 22, 2017, Art. no. 041011.

[27] V. Periyasamy and M. Pramanik, "Monte Carlo simulation of light transport in tissue for optimizing light delivery in photoacoustic imaging of the sentinel lymph node," *J. Biomed. Opt.*, vol. 18, 2013, Art. no. 106008.

[28] Y. Zhang, B. Chen, D. Li, and G.-X. Wang, "Efficient and accurate simulation of light propagation in bio-tissues using the three-dimensional geometric Monte Carlo method," *Numer. Heat Transfer A, Appl.*, vol. 68, pp. 827–846, 2015.

[29] D. Ruh, S. Subramanian, M. Theodor, H. Zappe, and A. Seifert, "Radiative transport in large arteries," *Biomed. Opt. Express*, vol. 5, p. 54, 2013.

[30] M. Hiraoka et al., "A Monte Carlo investigation of optical pathlength in inhomogeneous tissue and its application to near-infrared spectroscopy," *Phys. Med. Biol.*, vol. 38, pp. 1859–1876, 1993.

[31] Q. Fang, "Mesh-based Monte Carlo method using fast ray-tracing in Plücker coordinates," *Biomed. Opt. Express*, vol. 1, pp. 165–75, 2010.

[32] H. Li et al., "A mouse optical simulation environment (MOSE) to investigate bioluminescent phenomena in the living mouse with the Monte Carlo method 1," *Acad. Radiol.*, vol. 11, pp. 1029–1038, 2004.

[33] A. V. Gorshkov and M. Y. Kirillin, "Monte Carlo simulation of brain sensing by optical diffuse spectroscopy," *J. Comput. Sci.*, vol. 3, pp. 498–503, 2012.

[34] D. A. Boas, J. Culver, J. Stott, and A. Dunn, "Three dimensional Monte Carlo code for photon migration through complex heterogeneous media including the adult human head," *Opt. Express*, vol. 10, pp. 159–170, 2002.

[35] T. Binzoni, T. S. Leung, R. Giust, D. Rüfenacht, and A. H. Gandjbakhche, "Light transport in tissue by 3D Monte Carlo: Influence of boundary voxelization," *Comput. Methods Programs Biomed.*, vol. 89, pp. 14–23, 2008.

[36] S. V. Patwardhan, A. P. Dhawan, and P. A. Relue, "Monte Carlo simulation of light-tissue interaction: Three-dimensional simulation for trans-illumination-based imaging of skin lesions," *IEEE Trans. Biomed. Eng.*, vol. 52, no. 7, pp. 1227–1236, Jul. 2005.

[37] P. N. M. Božidar Šarler, P. Professor, P. Nithiarasu, D. Li, B. Chen, and G.-X. Wang, "Computational investigation on thermal responses of blood vessels during laser treatment of port wine stain," *Int. J. Numer. Methods Heat Fluid Flow*, vol. 26, pp. 534–555, 2016.

[38] M. A. L. Bell, X. Guo, D. Y. Song, and E. M. Boctor, "Transurethral light delivery for prostate photoacoustic imaging," *J. Biomed. Opt.*, vol. 20, 2015, Art. no. 036002.

[39] I. Ozden et al., "A coaxial optrode as multifunction write-read probe for optogenetic studies in non-human primates," *J. Neurosci. Methods*, vol. 219, pp. 142–154, 2013.

[40] R. Yao, X. Intes, and Q. Fang, "Generalized mesh-based Monte Carlo for wide-field illumination and detection via mesh retessellation," *Biomed. Opt. Express*, vol. 7, pp. 171–184, 2016.

[41] Y. Shin and H.-S. Kwon, "Mesh-based Monte Carlo method for fibre-optic optogenetic neural stimulation with direct photon flux recording strategy," *Phys. Med. Biol.*, vol. 61, pp. 2265–2282, 2016.

[42] D. Ancora, A. Zacharopoulos, J. Ripoll, and G. Zacharakis, "The role of cerebral spinal fluid in light propagation through the mouse head: Improving fluorescence tomography with Monte Carlo modeling," vol. 9700, *Proc. SPIE*, 2016, Art. no. 970015.

[43] R. Watté et al., "Modeling the propagation of light in realistic tissue structures with MMC-fpf: A meshed Monte Carlo method with free phase function," *Opt. Express*, vol. 23, pp. 17467–17486, 2015.

[44] L. Yue and M. S. Humayun, "Monte Carlo analysis of the enhanced transcranial penetration using distributed near-infrared emitter array," *J. Biomed. Opt.*, vol. 20, 2015, Art. no. 088001.

[45] A. E. Cerussi, N. Mishra, J. You, N. Bhandarkar, and B. Wong, "Monte Carlo modeling of light propagation in the human head for applications in sinus imaging," *J. Biomed. Opt.*, vol. 20, 2015, Art. no. 035004.

[46] S. Brigadoi, P. Aljabar, M. Kuklisova-Murgasova, S. R. Arridge, and R. J. Cooper, "A 4D neonatal head model for diffuse optical imaging of pre-term to term infants," *Neuroimage*, vol. 100, pp. 385–394, 2014.

[47] J. Chen, Q. Fang, and X. Intes, "Mesh-based Monte Carlo method in time-domain widefield fluorescence molecular tomography," *J. Biomed. Opt.*, vol. 17, 2012, Art. no. 106009.

[48] Q. Fang and D. A. Boas, "Monte Carlo simulation of photon migration in 3D turbid media accelerated by graphics processing units," *Opt. Express*, vol. 17, pp. 20178–20190, 2009.

[49] E. Margallo-Balbás and P. J. French, "Shape based Monte Carlo code for light transport in complex heterogeneous tissues," *Opt. Express*, vol. 15, pp. 14086–14098, 2007.

[50] T. Yamamoto and H. Sakamoto, "Frequency domain optical tomography using a Monte Carlo perturbation method," *Opt. Commun.*, vol. 364, pp. 165–176, Apr. 2016.

[51] V. Periyasamy and M. Pramanik, "Importance sampling-based Monte Carlo simulation of time-domain optical coherence tomography with embedded objects," *Appl. Opt.*, vol. 55, pp. 2921–2929, 2016.

[52] I. Krasnikov, C. Suhr, A. Seteikin, B. Roth, and M. Meinhardt-Wollweber, "Two efficient approaches for modeling of Raman scattering in homogeneous turbid media," *J. Opt. Soc. Amer. A*, vol. 33, pp. 426–433, 2016.

[53] L. V. Wang, S. L. Jacques, and L. Zheng, "CONV–convolution for responses to a finite diameter photon beam incident on multi-layered tissues," *Comput. Methods Programs Biomed.*, vol. 54, pp. 141–150, 1997.

[54] P. Naglič, F. Pernuš, B. Likar, and M. Bürmen, "Limitations of the commonly used simplified laterally uniform optical fiber probe-tissue interface in Monte Carlo simulations of diffuse reflectance," *Biomed. Opt. Express*, vol. 6, pp. 3973–3988, 2015.

[55] K. Sivasubramanian, V. Periyasamy, K. K. Wen, and M. Pramanik, "Optimizing light delivery through fiber bundle in photoacoustic imaging with clinical ultrasound system: Monte Carlo simulation and experimental validation," *J. Biomed. Opt.*, vol. 22, 2017, Art. no. 041008.

[56] B. H. Hokr et al., "Accurately modeling Gaussian beam propagation in the context of Monte Carlo techniques," *Proc. SPIE*, vol. 9706, 2016, Art. no. 970614.

[57] B. H. Hokr *et al.*, "Modelling focusing Gaussian beams in a turbid medium with Monte Carlo simulation," *Opt. Express*, vol. 23, pp. 8699–8705, 2015.

[58] I. N. Dolganova, A. S. Neganova, K. G. Kudrin, K. I. Zaytsev, and I. V. Reshetov, "Monte Carlo simulation of optical coherence tomography signal of the skin nevus," *J. Phys., Conf. Series*, vol. 673, 2014, Art. no. 012014.

[59] S. Malektaji, I. T. Lima, Jr., and S. S. Sherif, "Monte Carlo simulation of optical coherence tomography for turbid media with arbitrary spatial distributions," *J. Biomed. Opt.*, vol. 19, Apr. 2014, Art. no. 046001.

[60] I. T. Lima, A. Kalra, and S. S. Sherif, "Improved importance sampling for Monte Carlo simulation of time-domain optical coherence tomography," *Biomed. Opt. Express*, vol. 2, pp. 1069–1081, May 2011.

[61] G. Yao and L. H. V. Wang, "Monte Carlo simulation of an optical coherence tomography signal in homogeneous turbid media," *Phys. Med. Biol.*, vol. 44, pp. 2307–2320, Sep. 1999.

[62] B. H. Hokr, V. V. Yakovlev, and M. O. Scully, "Efficient time-dependent Monte Carlo simulations of stimulated raman scattering in a turbid medium," *ACS Photon.*, vol. 1, pp. 1322–1329, 2014.

[63] M. D. Keller, R. H. Wilson, M.-A. Mycek, and A. Mahadevan-Jansen, "Monte Carlo model of spatially offset Raman spectroscopy for breast tumor margin analysis," *Appl. Spectrosc.*, vol. 64, pp. 607–614, 2010.

[64] C. Wang *et al.*, "Acquiring reflective polarization from arbitrary multi-layer surface based on Monte Carlo simulation," *Opt. Express*, vol. 24, pp. 9397–411, May 2016.

[65] Y. Zhang, B. Chen, and D. Li, "Propagation of polarized light in the biological tissue: A numerical study by polarized geometric Monte Carlo method," *Appl. Opt.*, vol. 55, 2016, Art. no. 2681.

[66] M. Milanic, L. A. Paluchowski, and L. L. Randeberg, "Hyperspectral imaging for detection of arthritis: Feasibility and prospects," *J. Biomed. Opt.*, vol. 20, 2015, Art. no. 096011.

[67] N. Ortega-Quijano, F. Fanjul-Vélez, I. Salas-García, and J. L. Arce-Diego, "Polarized light Monte Carlo analysis of birefringence-induced depolarization in biological tissues," *Proc. SPIE*, vol. 8803, 2013, Art. no. 88030T.

[68] M. Ney and I. Abdulhalim, "Comprehensive Monte-Carlo simulator for optimization of imaging parameters for high sensitivity detection of skin cancer at the THz," *Proc. SPIE*, vol. 9721, 2016, Art. no. 97210W.

[69] M. Ney and I. Abdulhalim, "Ultrahigh polarimetric image contrast enhancement for skin cancer diagnosis using InN plasmonic nanoparticles in the terahertz range," *J. Biomed. Opt.*, vol. 20, 2015, Art. no. 125007.

[70] E. Pickwell, B. E. Cole, A. J. Fitzgerald, V. P. Wallace, and M. Pepper, "Simulation of terahertz pulse propagation in biological systems," *Appl. Phys. Lett.*, vol. 84, 2004, Art. no. 2190.

[71] G. C. Walker *et al.*, "Two methods for modelling the propagation of terahertz radiation in a layered structure," *J. Biol. Phys.*, vol. 29, pp. 141–148, 2003.

[72] V. L. Kuzmin, M. T. Neidrauer, D. Diaz, and L. A. Zubkov, "Diffuse photon density wave measurements and Monte Carlo simulations," *J. Biomed. Opt.*, vol. 20, 2015, Art. no. 105006.

[73] M. Testorf, U. Österberg, B. Pogue, and K. Paulsen, "Sampling of time- and frequency-domain signals in Monte Carlo simulations of photon migration," *Appl. Opt.*, vol. 38, pp. 236–245, 1999.

[74] G. Hennig *et al.*, "Non-invasive detection of iron deficiency by fluorescence measurement of erythrocyte zinc protoporphyrin in the lip," *Nature Commun.*, vol. 7, 2016, Art. no. 10776.

[75] D. Holt *et al.*, "Intraoperative near-infrared fluorescence imaging and spectroscopy identifies residual tumor cells in wounds," *J. Biomed. Opt.*, vol. 20, 2015, Art. no. 076002.

[76] A. Doronin, L. Tchvialeva, I. Markhvida, T. K. Lee, and I. Meglinski, "Backscattering of linearly polarized light from turbid tissue-like scattering medium with rough surface," *J. Biomed. Opt.*, vol. 21, 2016, Art. no. 071117.

[77] Y. Ryu, Y. Shin, D. Lee, J. Y. Altarejos, E. Chung, and H.-S. Kwon, "Lensed fiber-optic probe design for efficient photon collection in scattering media," *Biomed. Opt. Express*, vol. 6, pp. 191–210, 2015.

[78] A. V. Gorshkov and M. Y. Kirillin, "Acceleration of Monte Carlo simulation of photon migration in complex heterogeneous media using Intel many-integrated core architecture," *J. Biomed. Opt.*, vol. 20, 2015, Art. no. 085002.

[79] S. J. Wirkert *et al.*, "Robust near real-time estimation of physiological parameters from megapixel multispectral images with inverse Monte Carlo and random forest regression," *Int. J. Comput. Assisted Radiol. Surgery*, vol. 11, pp. 909–917, 2016.

[80] P. Naglič, F. Pernuš, B. Likar, and M. Bürmen, "Estimation of optical properties by spatially resolved reflectance spectroscopy in the subdiffusive regime," *J. Biomed. Opt.*, vol. 21, 2016, Art. no. 095003.

[81] Y. Liu, H. Jiang, and Z. Yuan, "Two schemes for quantitative photoacoustic tomography based on Monte Carlo simulation," *Med. Phys.*, vol. 43, pp. 3987–3997, 2016.

[82] Q. Liu and N. Ramanujam, "Scaling method for fast Monte Carlo simulation of diffuse reflectance spectra from multilayered turbid media," *J. Opt. Soci. Amer. A*, vol. 24, pp. 1011–1025, Apr. 2007.

[83] E. Alerstam, T. Svensson, and S. Andersson-Engels, "Parallel computing with graphics processing units for high-speed Monte Carlo simulation of photon migration," *J. Biomed. Opt.*, vol. 13, 2008, Art. no. 060504.

[84] S.-H. Hung, M.-Y. Tsai, B.-Y. Huang, and C.-H. Tu, "A platform-oblivious approach for heterogeneous computing: A case study with Monte Carlo-based simulation for medical applications," in *Proc. 2016 ACM/SIGDA Int. Symp. Field-Program. Gate Arrays*, 2016, pp. 42–47.

[85] P. Subochev, A. Orlova, I. Mikhailova, N. Shilyagina, and I. Turchin, "Simultaneous in vivo imaging of diffuse optical reflectance, optoacoustic pressure, and ultrasonic scattering," *Biomed. Opt. Express*, vol. 7, pp. 3951–3957, 2016.

[86] J. Cassidy, L. Lilge, and V. Betz, "Fast, power-efficient biophotonic simulations for cancer treatment using FPGAs," *IEEE 22nd Annu. Int. Symp. Field-Program. Custom Comput. Mach.*, 2014, pp. 133–140.

[87] J. Cassidy, L. Lilge, and V. Betz, "FullMonte: A framework for high-performance Monte Carlo simulation of light through turbid media with complex geometry," *Proc. SPIE*, 2013, vol. 8592, 2013, Art. no. 85920H.

[88] M. R. Escobar, I. S. Malektaji, I. T. Lima, and S. S. Sherif, "Accelerated simulation of optical coherence tomography of objects with arbitrary spatial distributions," *Proc. SPIE*, vol. 9288, 2014, Art. no. 928818.

[89] C. L. Campbell, K. Wood, C. T. Brown, and H. Moseley, "Monte Carlo modelling of photodynamic therapy treatments comparing clustered three dimensional tumour structures with homogeneous tissue structures," *Phys. Med. Biol.*, vol. 61, pp. 4840–4854, Jun. 2016.

[90] B. Arnal *et al.*, "Sono-photoacoustic imaging of gold nanoemulsions: Part I. Exposure thresholds," *Photoacoustics*, vol. 3, pp. 3–10, 2015.

[91] G. Held, S. Preisser, H. G. Akarçay, S. Peeters, M. Frenz, and M. Jaeger, "Effect of irradiation distance on image contrast in epi-optoacoustic imaging of human volunteers," *Biomed. Opt. Express*, vol. 5, pp. 3765–3780, 2014.

[92] I. Shlivko *et al.*, "Identification of layers in optical coherence tomography of skin: Comparative analysis of experimental and Monte Carlo simulated images," *Skin Res. Technol.*, vol. 21, pp. 419–425, 2015.

[93] J. Li, X. Zhang, L. Qiu, and D. F. Leotta, "An upgraded camera-based imaging system for mapping venous blood oxygenation in human skin tissue," *Opt. Commun.*, vol. 370, pp. 276–282, 2016.

[94] C.-W. Wei *et al.*, "Real-time integrated photoacoustic and ultrasound (PAUS) imaging system to guide interventional procedures: Ex vivo study," *IEEE Trans. Ultrason., Ferroelect., Freq. Control*, vol. 62, no. 2, pp. 319–328, Feb. 2015.

[95] T. F. Chen, G. V. Baranoski, B. W. Kimmel, and E. Miranda, "Hyperspectral modeling of skin appearance," *ACM Trans. Graph.*, vol. 34, 2015, Art. no. 31.

[96] Y. Zhou, W. Xing, K. I. Maslov, L. A. Cornelius, and L. V. Wang, "Handheld photoacoustic microscopy to detect melanoma depth in vivo," *Opt. Lett.*, vol. 39, pp. 4731–4734, 2014.

[97] Y. Ma *et al.*, "Wide-field optical mapping of neural activity and brain haemodynamics: Considerations and novel approaches," *Phil. Trans. R. Soc. B*, vol. 371, 2016, Art. no. 20150360.

[98] A. Vrana, M. L. Meier, S. Hotz-Boendermaker, B. K. Humphreys, and F. Scholkmann, "Cortical sensorimotor processing of painful pressure in patients with chronic lower back pain—An optical neuroimaging study using fNIRS," *Frontiers Human Neurosci.*, vol. 10, 2016, Art. no. 578.

[99] L. A. Hardy, C. H. Chang, E. M. Myers, M. J. Kennelly, and N. M. Fried, "Computer simulations of thermal tissue remodeling during transvaginal and transurethral laser treatment of female stress urinary incontinence," *Lasers Surg. Med.*, vol. 49, pp. 198–205, 2016.

[100] P. D. Kumavor *et al.*, "Co-registered pulse-echo/photoacoustic transvaginal probe for real time imaging of ovarian tissue," *J. Biophoton.*, vol. 6, pp. 475–484, 2013.

[101] S. Tang, J. Chen, P. Samant, K. Stratton, and L. Xiang, "Transurethral photoacoustic endoscopy for prostate cancer: A simulation study," *IEEE Trans. Med. Imag.*, vol. 35, no. 7, pp. 1780–1787, Jul. 2016.

[102] S. H. El-Gohary, M. K. Metwally, S. Eom, S. H. Jeon, K. M. Byun, and T.-S. Kim, "Design study on photoacoustic probe to detect prostate cancer using 3D Monte Carlo simulation and finite element method," *Biomed. Eng. Lett.*, vol. 4, pp. 250–257, 2014.

[103] J.-M. Yang, C. Li, R. Chen, Q. Zhou, K. K. Shung, and L. V. Wang, "Catheter-based photoacoustic endoscope," *J. Biomed. Opt.*, vol. 19, 2014, Art. no. 066001.

[104] H. Jia, B. Chen, D. Li, and Y. Zhang, "Boundary discretization in the numerical simulation of light propagation in skin tissue: Problem and strategy," *J. Biomed. Opt.*, vol. 20, 2015, Art. no. 025007.

[105] D. S. Jung, J. A. Crowe, J. P. Birchall, M. G. Somekh, and C. W. See, "Anti-confocal versus confocal assessment of the middle ear simulated by Monte Carlo methods," *Biomed. Opt. Express*, vol. 6, pp. 3820–3825, 2015.

[106] B. Shi, Z. Meng, L. Wang, and T. Liu, "Monte Carlo modeling of human tooth optical coherence tomography imaging," *J. Opt.*, vol. 15, 2013, Art. no. 075304.

[107] D. Tendeiro, G. Lopes, P. Vieira, and J. P. Santos, "Monte Carlo simulation of laser beams interaction with the human eye using Geant4," *Biomed. Eng. Online*, vol. 13, 2014, Art. no. 58.

[108] P.-Y. Huang, C.-Y. Chien, C.-R. Sheu, Y.-W. Chen, and S.-H. Tseng, "Light distribution modulated diffuse reflectance spectroscopy," *Biomed. Opt. Express*, vol. 7, 2016, Art. no. 2118.

[109] A. Mowla *et al.*, "Concurrent reflectance confocal microscopy and laser doppler flowmetry to improve skin cancer imaging: A Monte Carlo model and experimental validation," *Sensors*, vol. 16, 2016, Art. no. E1411.

[110] T. Strömberg, H. Karlsson, I. Fredriksson, F. H. Nyström, and M. Larsson, "Microcirculation assessment using an individualized model for diffuse reflectance spectroscopy and conventional laser Doppler flowmetry," *J. Biomed. Opt.*, vol. 19, 2014, Art. no. 057002.

[111] I. Fredriksson, M. Larsson, and T. Strömberg, "Optical microcirculatory skin model: Assessed by Monte Carlo simulations paired with in vivo laser Doppler flowmetry," *J. Biomed. Opt.*, vol. 13, 2008, Art. no. 014015.

[112] S. L. Jacques, "Coupling 3D Monte Carlo light transport in optically heterogeneous tissues to photoacoustic signal generation," *Photoacoustics*, vol. 2, pp. 137–142, 2014.

[113] P. Lundin *et al.*, "Noninvasive monitoring of gas in the lungs and intestines of newborn infants using diode lasers: Feasibility study," *J. Biomed. Opt.*, vol. 18, 2013, Art. no. 127005.

[114] Q. Fang, "Comment on "A study on tetrahedron-based inhomogeneous Monte-Carlo optical simulation"," *Biomed. Opt. Exp.*, vol. 2, pp. 1258–1264, 2011.

[115] H. Shen and G. Wang, "A study on tetrahedron-based inhomogeneous Monte Carlo optical simulation," *Biomed. Opt. Exp.*, vol. 2, pp. 44–57, 2011.

[116] L. Wang, S. Ren, and X. Chen, "Comparative evaluations of the Monte Carlo based light propagation simulation packages for optical imaging," *J. Innov. Opt. Health Sci.*, 2017, doi:10.1142/S1793545817500171.

[117] B. Majaron, M. Milanic, and J. Premru, "Monte Carlo simulation of radiation transport in human skin with rigorous treatment of curved tissue boundaries," *J. Biomed. Opt.*, vol. 20, 2015, Art. no. 015002.

[118] J. Selb, T. M. Ogden, J. Dubb, Q. Fang, and D. A. Boas, "Comparison of a layered slab and an atlas head model for Monte Carlo fitting of time-domain near-infrared spectroscopy data of the adult head," *J. Biomed. Opt.*, vol. 19, 2014, Art. no. 016010.

[119] X. Yang, G. Li, and L. Lin, "Determination of photon quantity in Monte Carlo simulation," *Opt. Quant.Electron.*, vol. 48, 2016, Art. no. 422.

[120] A. Sassaroli and F. Martelli, "Equivalence of four Monte Carlo methods for photon migration in turbid media," *J. Opt. Soc. Amer. A*, vol. 29, pp. 2110–2117, 2012.

[121] J. M. Stujenske, T. Spellman, and J. A. Gordon, "Modeling the spatiotemporal dynamics of light and heat propagation for in vivo optogenetics," *Cell Rep.*, vol. 12, pp. 525–534, 2015.

[122] A. Glaser, Y. Wang, and J. Liu, "Assessing the imaging performance of light sheet microscopies in highly scattering tissues," *Biomed. Opt. Exp.*, vol. 7, pp. 454–466, 2016.

[123] Y. Liu, S. L. Jacques, M. Azimipour, J. D. Rogers, R. Pashaie, and K. W. Eliceiri, "OptogenSIM: A 3D Monte Carlo simulation platform for light delivery design in optogenetics," *Biomed. Opt. Express*, vol. 6, 2015, Art. no. 4859.

[124] Y. H. Ong and T. C. Zhu, "Analytic function for predicting light fluence rate of circular fields on a semi-infinite turbid medium," *Opt. Express*, vol. 24, pp. 26261–26281, 2016.

[125] Y. Lou, K. Wang, A. A. Oraevsky, and M. A. Anastasio, "Impact of non-stationary optical illumination on image reconstruction in optoacoustic tomography," *J. Opt. Soc. Amer. A*, vol. 33, pp. 2333–2347, 2016.

[126] D. Yang, X. Chen, X. Cao, J. Wang, J. Liang, and J. Tian, "Performance investigation of SP3 and diffusion approximation for three-dimensional whole-body optical imaging of small animals," *Med. Biol. Eng. Comput.*, vol. 53, pp. 805–814, Sep. 2015.

[127] D. Wangpraseurt, S. L. Jacques, T. Petrie, and M. Kühl, "Monte Carlo modeling of photon propagation reveals highly scattering coral tissue," *Frontiers Plant Sci.*, vol. 7, 2016, Art. no. 1404.

[128] P. Matousek, C. Conti, C. Colombo, and M. Realini, "Monte Carlo simulations of subsurface analysis of painted layers in micro-scale spatially offset Raman spectroscopy," *Appl. Spectrosc.*, vol. 69, pp. 1091–1095, 2015.

[129] Y. Lou, W. Zhou, T. P. Matthews, C. M. Appleton, and M. A. Anastasio, "Generation of anatomically realistic numerical phantoms for photoacoustic and ultrasonic breast imaging," *J. Biomed. Opt.*, vol. 22, 2017, Art. no. 041015.

Vijitha Periyasamy received the bachelor's degree in medical electronics from Visvesvaraya Technological University, Belgaum, India.

She is with the research staff at the School of Chemical and Biomedical Engineering, Nanyang Technological University, Singapore. Her research interests include biomedical image processing for clinical evaluation, development of multimodal imaging systems, Monte Carlo simulation for light transport in biological tissue, and application of bioengineering for different medical practice systems.

Manojit Pramanik received the Ph.D. degree in biomedical engineering from Washington University, St. Louis, MO, USA.

He is an Assistant Professor in the School of Chemical and Biomedical Engineering, Nanyang Technological University, Singapore. His research interests include the development of photoacoustic/thermoacoustic imaging systems, image reconstruction methods, clinical application areas such as breast cancer imaging, molecular imaging, contrast agent development, and Monte Carlo simulation of light propagation in biological tissue.